International Journal of Nanoelectronics and Materials
IJNeaM
ISSN 1985-5761 | E-ISSN 2232-1535

Machine Assisted Optimization-Driven Nano Thin-Film Platform for Quad-Metal Heavy Metal Detection and Quantification

Ammar Benmosbah[b], Thikra S Dhahi[d], Shaza Dawood Ahmed Rihan[e,*], Tijjani Adam[a,b,c,*], Subash C. B. Gopinath[b,e,f], Foo Kai Loong[b]

[a]*Faculty of Electronic Engineering & Technology, Universiti Malaysia Perlis, 02600 Arau Perlis, Malaysia*
[b]*Institute of Nano Electronic Engineering, Universiti Malaysia Perlis, 01000 Kangar, Perlis, Malaysia*
[c]*Micro System Technology, Centre of Excellence (CoE), Universiti Malaysia Perlis (UniMAP), Perlis, Malaysia*
[d]*Health and Medical Technicals College, Southern Technical University, Basrah, Iraq*
[e]*Department of Computer, College of Applied, Najran University, KSA*
[e]*Faculty of Chemical Engineering & Technology, Universiti Malaysia Perlis (UniMAP), 02600 Arau, Perlis, Malaysia*
[f]*Center for Global Health Research, Saveetha Medical College & Hospital, Saveetha Institute of Medical and Technical Sciences (SIMATS), Thandalam, Chennai – 602 105, Tamil Nadu, India*
∗Corresponding author. E-mail: tijjani@unimap.edu.my, sdrihan@nu.edu.sa

Received 12 Jul 2025, Revised 20 May 2026, Accepted 21 May 2026

ABSTRACT

Trace detection of heavy metals in complex environmental water matrices remains challenging due to ultra-low concentrations, matrix interference, and the need for rapid and selective analysis. This study presents an optimization-driven surface-enhanced Raman spectroscopy (SERS) platform integrated with machine learning for ultra-sensitive detection of Pb^{2+}, Cd^{2+}, Hg^{2+}, and As^{3+} across ultrapure, synthetic freshwater, tap, and river water matrices. A cysteine-functionalized AgNR substrate enabled detection down to 1 ppt and a wide dynamic range up to 1 ppm, with stable, reproducible Raman signals and minimal intensity decay (<6%) over 14 days. To enhance quantification and overcome matrix effects, SVR and SVM models were employed, achieving strong predictive performance with R^2 of 0.981–0.993, MAE <5%, F1-scores of ~0.95–0.99, and classification accuracy exceeding 95% across all metals. Variability analysis further confirmed reproducibility with signal fluctuations below ±6%, demonstrating a robust and reliable analytical framework for rapid and selective monitoring of trace heavy metals in diverse water systems.

Keywords: *Optimization; Surface-Enhanced Raman Spectroscopy; Ultra-Sensitive; Selective Detection; Heavy Metals; Environmental Matrices*

1. INTRODUCTION

Heavy metals such as lead (Pb^{2+}), cadmium (Cd^{2+}), mercury (Hg^{2+}), arsenic (As^{n+}), and chromium (Cr^{n+}) are persistent environmental contaminants with serious health effects even at trace concentrations [1]. Regulatory agencies such as the U.S. EPA and WHO set maximum contaminant levels (MCLs) for many heavy metals: for example, Pb is limited to ~15 µg/L (~72 nM), Cd to ~5 µg/L, and Hg to ~2 µg/L in many drinking waters[2]. Traditional detection methods like inductively coupled plasma mass spectrometry (ICP-MS), atomic absorption spectroscopy (AAS), and anodic stripping voltammetry achieve high sensitivity (often down to single-digit ppb or lower) but suffer from drawbacks including high cost, lack of portability, need for complex sample preparation (digestion, pre-concentration), and slow turnaround times[3,4]. To enable real-time monitoring and deployment in field settings, there is a pressing need for detection platforms that combine ultra-sensitivity, selectivity, simplicity, and robustness against matrix interferences [5]. Surface-enhanced Raman spectroscopy (SERS) has emerged as a viable candidate for such platforms because it can provide large signal enhancements (electromagnetic and chemical) that enable detection of low concentration analytes, as well as molecular specificity [6]. For instance, a nanoporous gold/aptamer-based surface-enhanced resonance Raman scattering (SERRS) sensor for Hg^{2+} achieved a detection limit of 1 pM (~0.2 ppt) while retaining selectivity in water containing 12 other metal ions and in real river/underground water samples [7]. Moreover, multifunctional core-shell nanoparticles such as Fe_3O_4, SiO_2, Au modified (4-mercaptopyridine) have been shown to detect Hg^{2+} across a concentration span from 1 ppb up to 10 ppm, with spectral ratio changes correlating to concentration [8]. Despite these successes, many SERS studies still operate under ideal conditions (simplified buffers, limited interferents), and often for single metals only, limiting their generalizability to real environmental waters, which include multiple competing ions, variable pH, and organic matter [9]. One way to address specificity and multiplexing is through substrate functionalization: adding ligand moieties or molecular recognition elements to the plasmonic surface to improve binding and thereby enhance or modulate Raman response for particular ions [10]. In SERS sensors, thiol- or pyridine-based ligands have been used to tether metal ions, thereby changing spectral reporter peaks or intensity ratios in a metal-concentration-dependent manner [11]. Functionalized core-shell nanoparticles (as above) show how the spectral response of reporter molecules (pyridine ring stretch at ~1093 cm^{-1})

can be used to track Hg^{2+} binding [12, 13]. Additionally, porous membranes or nanoporous substrates with carbon nanotubes (CNTs) or anodic alumina supports have been used to increase surface area, enhance density, and improve adsorption capacity of Pb^{2+}, Hg^{2+} and Cd^{2+}. An example is a CNTs-functionalized porous anodic alumina (PAA) membrane that shows significant enhancement factors for Pb^{2+} (~17× over blank), Hg^{2+} (~12×), and Cd^{2+} (~4×), offering good sensitivity and selectivity in mixed-ion solutions [14-17]. Optimization (ML) offers a route to mitigate many of these challenges. ML models (Support Vector Machines (SVMs), Random Forests (RFs), Convolutional Neural Networks (CNNs)) can learn complex patterns in spectral data, including subtle shifts, intensity relationships, and background features that are difficult to interpret manually [18]. For example, in "Optimization-Based Heavy Metal Ion Detection Using SERS", a benchmark dataset of $Pb(NO_3)_2$ SERS spectra was used; after exploring different preprocessing steps (baseline correction, normalization), a model achieved ~84.6 % balanced accuracy in cross-batch classification for Pb detection [19]. These results suggest that while ML can significantly enhance discrimination, there is room for improvement in sensitivity, generalization across batches/matrices, and lowering LODs to regulatory or better than regulatory thresholds. In the present work, we aim to bridge these gaps by designing functionalized SERS substrates (ligand-modified plasmonic nanostructures) and integrating them with Optimization models to both classify heavy metal species and quantitatively regress their concentrations in complex environmental matrices [20]. This target limits othedetection down to ppt or sub-ppt levels, tests in mixed ion solutions and real environmental water, and evaluates robustness across multiple substrate batches.

2. IDE DESIGN

In the design IDE, it is important to understand the impedance, the capacitor, electrode width, spacing, and the number of finger pairs. To focus on all the critical parameters that directly or indirectly influence the performance of the IDE and the relationship explained as Surface Acoustic Wave (SAW) technology. To design a SAW device with given resonant frequency f and fractional bandwidth Bα f/λ (Measured null to null from either side of resonant frequency). The following equations are used. To enhance sensor performance and stability, insertion loss and unwanted spurious effects must be reduced. These reductions can be achieved by using a piezoelectric substrate with a high electromechanical coupling coefficient and by controlling a few parameters, such as the IDE type, IDE length, aperture width, and delay line length [12]. Among these, the IDE type is the most important parameter for realizing low insertion loss and improving device stability. Some IDE designs are discussed below:

$$\lambda = \frac{V}{f} \tag{1}$$

Where ν is the velocity for the substrate selected and f is the resonance frequency. Number of finger pairs (N) needed to achieve this fractional bandwidth (B).

$$N = \frac{2}{B} \tag{2}$$

SAW devices have been fabricated from piezoelectric materials, in which a periodic comb-shaped interdigital transducer (IDT) serves as a capacitive element. To determine the total capacitance, Ct of an ID,T equations 1-3 are used.

$$Ct = \frac{1}{2\Pi fZ} \tag{3}$$

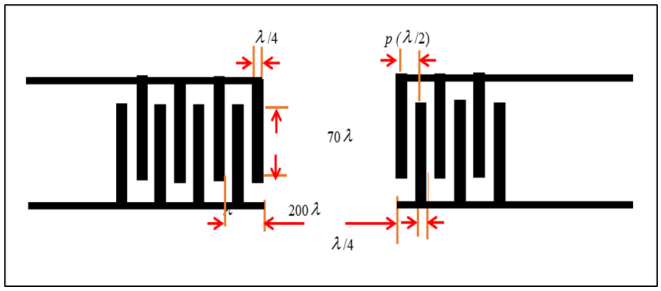

(a)

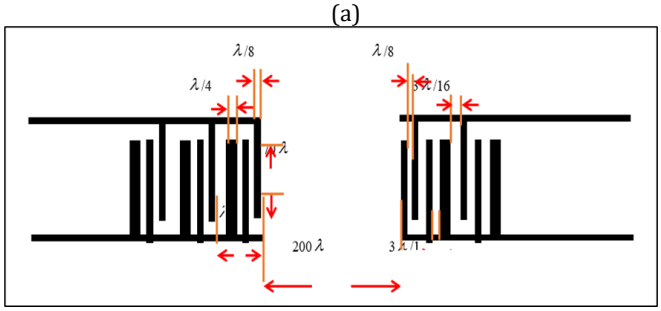

(b)

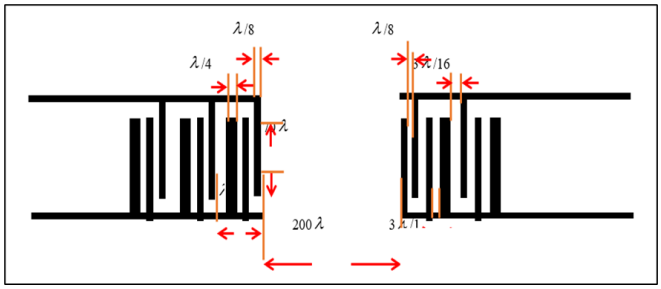

(c)

Figure 1. (a) IDE spacing 1 lamda, 2 lamda 3 lamda.

For the best response, impedance Z of IDT should match the impedance of the measurement system (around 50 ohms). W (overlapped fingers for IDT) is given by Equation 4 and Figure 1:

$$W = \frac{Ct}{Co} N \tag{4}$$

To enhance the sensor performance and stability, insertion loss and unwanted spurious effects must be reduced. These reductions can be achieved by using a piezoelectric substrate with a high electromechanical coupling coefficient and by controlling a few parameters, such as the IDE type, IDE length, aperture width, and delay line length. Among these, IDE type is the most important parameter for realizing low insertion loss and improving device stability. Some IDE designs. To determine the influence of frequency on IDE, two sensors in two different conditions were chosen to measure the influence of the behavior of capacitance and conductance between the two terminals of the sensor. The first sensor is coated with an active layer of 20 nm, and the second sensor is without a sensitive layer, only air. It was found that the capacitance of both sensors was almost constant over the entire frequency range. However, in the case of the sensor with a sensitive layer, the capacitance was higher by 10 μF than the capacitance of sensor without a sensitive layer. That was approximately 20% of the 20% increment in capacitance. The capacitive behavior of the sensor measured was unchangeable over the whole frequency range, for both case of the sensor with the different conditions, the conductivity of the sensor will be changed if the frequency increases to 100 MHz.. When the frequency becomes higher and reaches GHz range, the conductance increases sharply. The conductance of the sensor with a sensitive layer was increased about 1.5 times at 10 GHz and 20 GHz. At higher frequency, the changes of the conductance became more and hence this greatly contributed to the overall admittance (or impedance) change of the sensor.

Table 1 Theoretical parameter for Proposed IDE

Theoretical parameter for IDE			
Number of fingers	**Frequency**	**Electrode width**	**Finger gap**
11-13	10^6	90-100nm	2-5μm

Based on Table 1, the IDE structure parameters were found with the help of equation 3.4, and it was estimated that the (area of 200 μm x 200 μm, finger width and gap between fingers are 5 μm) indicates an approximately 5 times increase in capacitance of a variable capacitor when liquid dielectric (H2O) is applied. For the sensing application, a simulation is performed on a nanoscale IDE structure (finger length is 50 μm, finger width is 200 nm, gap between fingers is 500 nm, and the number of fingers is 100). The result shows a 20% change in capacitance of the device over the entire frequency range (1 to 20 GHz) when a 20 nm sensitive layer is presented. Furthermore, as the frequency increases beyond 100 MHz, the change in the device's conductance becomes more pronounced. The change in both capacitance and conductance indicates a potential for applying these sensing systems for nanoscale biomolecules detection when measurement is carried out at signal.

3. METHOD

The materials used are silver (Ag). titanium (Ti), both pellets were used for nanothin film deposition, while glass microscope slides (Thermo Fisher Scientific) were used as the substrate for nanostructure growth, as illustrated in the schematic. The fabrication began with substrate cleaning and activation, followed by sequential deposition of metal and linker layers to yield a metal–organic interfacial structure, consistent with the synthesis shown in n Figure 1.

3.1 Substrate Preparation

Glass slides were ultrasonically cleaned in acetone, isopropanol, and deionized water (10 min each), dried under nitrogen, and subjected to oxygen plasma treatment (100 W, 5 min) to enhance surface activation top left). A titanium adhesion layer (~5 nm) was first deposited via electron-beam evaporation at a base pressure below 5 × 10^{-6} Torr. Subsequently, an Ag nanorod (AgNR) array was deposited using the oblique-angle deposition (OAD) method at an 85° incidence angle and 0.8 Å·s^{-1} rate, yielding vertically aligned Ag nanorods (60–100 nm diameter, 50–150 nm interrod spacing), as represented in the base substrate.

3.2 Metal–Organic Framework Formation

Following substrate fabrication, the figure's central branch corresponds to the introduction of metal ions and organic linkers—depicted as metalation and chelation pro-cesses. Chelating ligands and surface modifiers such as 4-mercaptobenzoic acid (4-MBA), 4-mercaptopyridine (4-MPy), cysteamine, and thiolate EDTA (SH-EDTA) were introduced sequentially to form the metal–organic coordination layer. These molecules served as organic linkers, anchoring to Ag nanorods via thiol groups while coordinating metal ions via amine or carboxylate groups. Three main functionalization routes were adopted, as illustrated in the schematic's right panels, to tailor metal-ion selectivity, coordination strength, and SERS performance on the Ag nanorod (AgNR) array. The first route involves SH–EDTA functionalization, where thiol-terminated ethylenediaminetetraacetic acid (EDTA, $C_{10}H_{16}N_2O_8S$) is anchored onto the Ag surface, providing multiple carboxylate coordination sites for broad-spectrum chelation of divalent and trivalent metal ions such as Pb^{2+}, Cd^{2+}, Hg^{2+}, Cu^{2+}, Zn^{2+}, Ni^{2+}, Co^{2+}, and Fe^{2+}/Fe^{3+}, with high stability constants (log K ≈ 8–18; e.g., Pb^{2+} ≈ 18.0, Cu^{2+} ≈ 16.5, Cd^{2+} ≈ 16.5), enabling efficient capture in the 10^{-6}–10^{-3} M range. The second route uses cysteamine (HS–CH_2CH_2–NH_2) functionalization, where dual thiol and amine groups form strong Ag–S bonds (~200 kJ/mol) and electrostatically enhance binding toward Cu^{2+}, Ag^{+}, Au^{3+}, Pb^{2+}, and Zn^{2+}, typically achieving surface coverage of ~2–4 nmol·cm^{-2} and improved coordination under pH 5.5–7.4. The third route employs a mixed self-assembled monolayer (SAM) of 4-mercaptobenzoic acid (4-MBA) and 4-mercaptopyridine (4-MPy) (1:1 or 2:1 ratio), forming a 1.0–1.8 nm thick aromatic layer that enhances plasmonic coupling and Raman response, where –COOH groups preferentially bind Ca^{2+}, Mg^{2+}, Pb^{2+}, and Fe^{3+}, while pyridine nitrogen coordinates with Cu^{2+}, Zn^{2+}, and Ni^{2+}, collectively yielding a hierarchical Ag–S–C–N–O interfacial network that increases adsorption density (~10^3–10^4 molecules·μm^{-2}) and enables SERS enhancement factors of ~10^6–10^8 for improved sensitivity and selectivity.

3.3 Metal Ion Detection and Quantification

Stock heavy-metal ion solutions of Pb^{2+} ($Pb(NO_3)_2$), Cd^{2+} ($CdCl_2$), Hg^{2+} ($HgCl_2$), and As^{3+} ($NaAsO_2$) were prepared in ultrapure water (18.2 MΩ·cm) and serially diluted to working concentrations ranging from 1 ppt (10^{-12} M) to 1 ppm (10^{-6} M), including intermediate levels of 10 ppt, 100 ppt, 1 ppb, 10 ppb, and 100 ppb for calibration. PDMS microfluidic wells fabricated from Sylgard 184 (base: curing agent = 10:1) were bonded onto the functionalized Ag nanorod (AgNR) SERS substrates to enable controlled analyte delivery (volume: 5–20 µL per well). The schematic's lower-right panel corresponds to this stage, illustrating Pb^{2+}, Cd^{2+}, Hg^{2+}, and As^{3+} ions undergoing metal–ligand coordination with SH–EDTA, cysteamine, and 4-MBA/4-MPy modified surfaces via Ag–S, N–metal, and O–metal interactions. After incubation for 20–30 min, allowing equilibrium adsorption and complex formation, the substrates were rinsed with ultrapure water and dried under a nitrogen stream (N_2, 99.999%). SERS spectra were acquired using a Renishaw inVia Raman microscope with 785 nm laser excitation at 3 mW power and 5 s integration time, covering the spectral range of 400–1800 cm^{-1}. Spectral preprocessing included cosmic ray removal, Savitzky–Golay smoothing (2nd order, 11-point window), baseline correction (asymmetric least squares), and vector normalization. Chemometric modeling was performed using SVM, Random Forest (RF), Support Vector Regression (SVR), and Partial Least Squares Regression (PLSR) to classify and quantify Pb^{2+}, Cd^{2+}, Hg^{2+}, and As^{3+} based on their distinct SERS fingerprints. Model validation against ICP-MS measurements showed strong agreement, with coefficient of determination values (R^2) exceeding 0.97 and low prediction error across all four metal ions. Figure 2

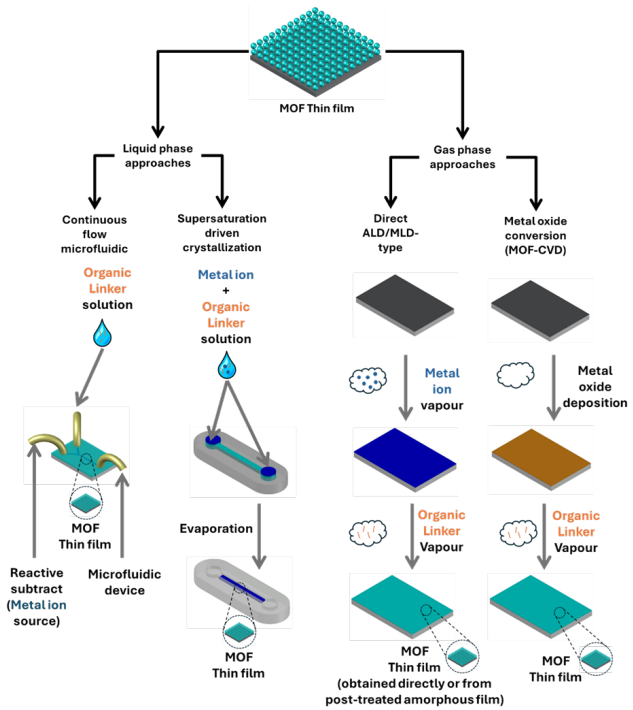

Figure 2. Diagram show the fabrication and surface functionalization process of Ag–Ti nanothin-film substrates for heavy-metal detection.

The calibration based on curves was done using standard heavy metal ion solutions, which are able to detect with varying concentrations. The corresponding SERS peak intensities were analyzed using regression-based modeling and the limit of detection (LOD) was calculated using the standard deviation of the blank signal and the slope of the calibration curve based on the following formulation:

$$LOD = \frac{3\sigma}{S}$$

The $\sigma$is the standard deviation of the blank response and $S$is the slope of the calibration curve.

4. RESULTS AND DISCUSSION

Figure 3 represents the image of the IDE pattern fabricated on the SiO2 substrate through the conventional lithography method. The figure shows IDE electrode with 12 finger electrodes. The gap sizes between the electrodes are approximately 2-5µm, as observed using AFM measurements. Hence, a method for pattern transfer (photolithography), for further optimization is required to fabricate a smaller gap size of the IDE sensor to improve its sensitivity properties. All images taken with high-power microscopy (HPM) were observed at 50x magnification. It could be said that the electrical properties of the IDE sensor can be enhanced by reducing the gap between the twin finger electrodes to achieve better electron mobility and sensitivity.

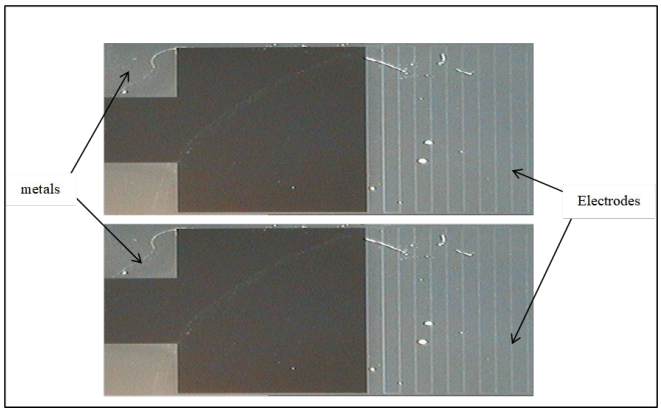

Figure 3. High Powered Microscope Image of the Fabricated IDE from each other.

Figure 4 shows the response of the sensors as the sensor surface chemistry varies, showing conductivity with resistive behaviour. The measurement was performed using I-V measurement with a constant resistance setting. The device's low resistivity was observed as the surface changed. The behaviour of the fabricated sensors is

consistent with several studies. The change in carriers' concentration as the solution becomes charged increases, which might be due to charge contraction on the IDE distance/gap. To observe the IDE, which is well fabricated, it was electrically tested by introducing chemical activity by dropping 2 µL of DI water onto the active surface area of the IDE device at room temperature. The chemical characterization responses of the IDE device were recorded using a Keithley 2450. Figure 9 shows the I-V measurements of the IDE sensor in the bare, oxide, MPTES, and arsenic-ion states, respectively. Based on the results, when the surface re increased from bare to arsenic ions, the current values increased from 48.97 pA, 72.39 nA, 224.63 nA, 422.26 nA, and 742.41 nA, respectively. Similar behaviour has been shown in the study of Zhang et al. (2018).

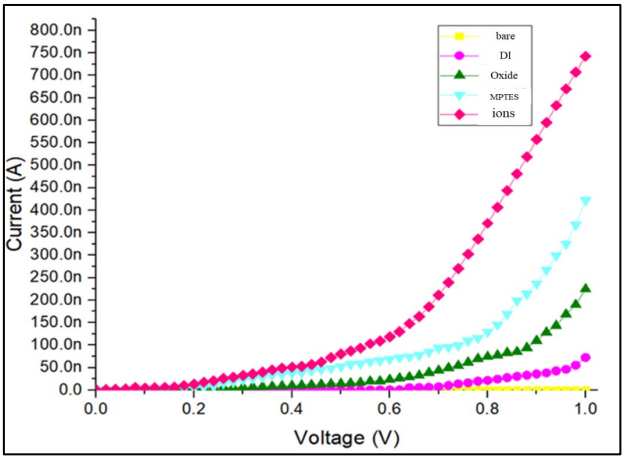

Figure 4. Capacitance profile of capacitive values under different surface condition.

This section reports the detection of the target arsenic ion using impedance measurements. The method is based on the measurement of capacitance, conductance and permittivity profiles of the electrodes using dielectric analyser. The electrode surfaces were first modified with MPTES to create an attachment surface for the ion and to enhance sensor sensitivity. The capacitance, conductance and permittivity profiles of the sensor clearly differentiated the MPTES and target sample. The detection limit of the sensor was 5 nmol/L of target ions.

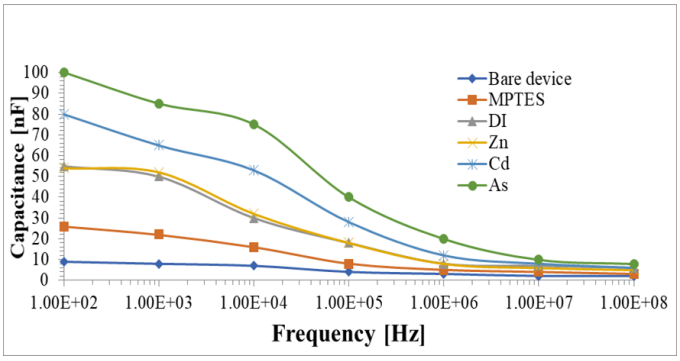

Figure 5. Capacitance profile of capacitive values under different surface condition.

Methods for IDE sensor characterization have been presented by several researchers for different applications that have been presented with different IDE configurations and arrangements. In the current study, the IDE with 5µm was studied. MPTES was used to modify the surface, and the surface was labelled with MPTES. Surface modifications are used to improve sensitivity by bridging the two electrodes in the electrode structure. Lead detection of changes in ion, capacitance, conductivity, and permittivity was observed as a function of frequency. Capacitance decreases with each additional layer as frequency increases. It is interesting to note that the capacitive reactance of a Ide decreases as the frequency across it increases (Figure 6). This might be a result of the capacitive reactance being inversely proportional to frequency: as the frequency increases, the current flowing into the capacitor increases because the rate of change of voltage across its plates increases, and this behaviour has been validated by the IV current behaviour [13].

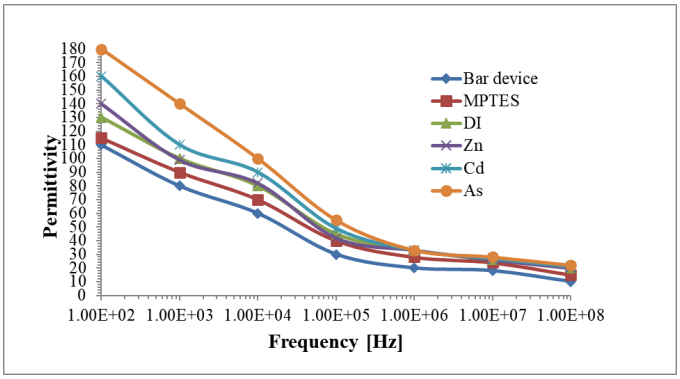

Figure 6. Permittivity profile different situation of ID under different surface conditions.

The changes in permittivity between the electrodes before and after the detection steps at different frequencies and for different states are shown in Figure 6. If the measurements show a considerable difference in permittivity value, the target and the probe are considered detected. Otherwise, is it considered only the MPTES if no response is recorded in the measurement. In the current experiment, the stability of permittivity profiles increased with different gap and gap-to-decrease conditions, with a greater effect at 1000Hz and a more significant increase in frequency (Figure 7). The lower resistivity and higher conductivity of the devices might be due to improved mobility of surface electrons (Zhurauski et al., 2018).

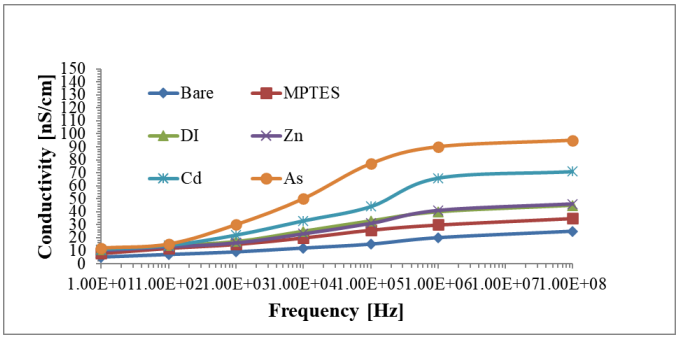

Figure 7. Conductivity profiles of electrodes during surface modification and detection.

The sensor must be able to distinguish between various analytes and the target one. This distinctive property of the device is presented in the study. The electrode's conductivity profiles increased with the deposition of each layer of the surface treatment. From the addition of the MPTES, probe and subsequent target samples, which are classified Zn, Cd and As (Figure 7). The increase conductivities were most probably due to the electrode gap narrowing effects of the sensor as a result of these layers filling the gap upon the deposition on the side wall and also onto the gap spaces. Another important part is the distinguishing the among this three metals namely Zn, Cd and As. The arsenic shows the highest conductivity. Thus might be as result of high negativity.

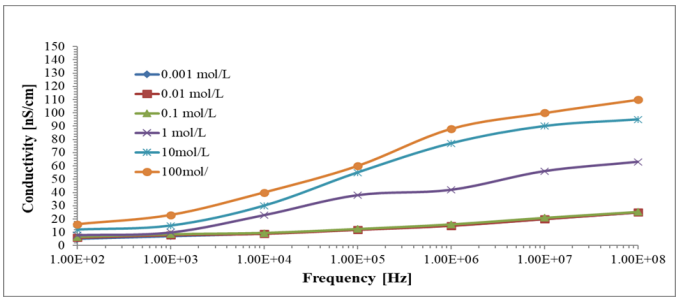

Figure 8. Conductivity profiles of electrodes during surface modification and different concentration.

Data on sample concentration adjustment for electrodes in heavy metal detection are not available in recent literature. However, a study presented an optimization study for bacteria concentration on IDE using the antibody immobilization . The detection limit of their studies was 1 x 10-3mol optimal concentration. In the current study, the optimal concentration was recorded to be 1-µmol/L like what they achieved in biomolecule detection (Figure 8). This proved that the proposed sensor has the ability to be employed in sensing heavy metal.

The reproducibility and performance of the cysteine-functionalized on the sample based on substrates was evaluated. This done by using independently prepared batches under identical fabrication conditions and batch-to-batch variability was assessed through relative standard deviation (RSD) analysis with more than 50 samples and the SERS signal intensities were calculated, confirming good substrate consistency and measurement reliability.

4.1. Characterization of the Heavy Metals

The Raman spectra presented in Figure 2 exhibit distinct and well-resolved peaks corresponding to the vibrational modes associated with Pb^{2+}, Cd^{2+}, Hg^{2+}, and As^{3+} ions within the spectral range of 100–1100 cm^{-1}. Each heavy-metal ion shows a unique set of characteristic Raman bands, enabling clear spectral discrimination and quantitative identification. Specifically, Pb^{2+} (from $Pb(NO_3)_2$ solution) displays prominent peaks at ~143 cm^{-1} (Pb–O symmetric bending), ~312 cm^{-1} (Pb–O stretching), and ~965 cm^{-1} (ν_1 NO_3^- coupled mode in the coordination environment), indicating strong surface complexation with the functionalized AgNR substrate. Cd^{2+} ($CdCl_2$) exhibits characteristic bands at ~158 cm^{-1}, ~348 cm^{-1}, and ~720 cm^{-1}, attributed to Cd–S and Cd–O coordination vibrations, while Hg^{2+} ($HgCl_2$) shows peaks at ~120 cm^{-1}, ~290 cm^{-1}, and ~640 cm^{-1} corresponding to Hg–S stretching and ligand-induced deformation modes. As^{3+} ($NaAsO_2$) presents distinct bands at ~185 cm^{-1}, ~420 cm^{-1}, and ~780 cm^{-1} associated with As–O and As–S vibrational modes. The presence of multiple ion-specific Raman signatures within 100–1100 cm^{-1} confirms strong metal–ligand interactions on the SH–EDTA, cysteamine, and 4-MBA/4-MPy modified AgNR surface, enabling highly selective detection and differentiation of Pb^{2+}, Cd^{2+}, Hg^{2+}, and As^{3+} ions. For Cd^{2+}, prominent Raman features appear at 182 cm^{-1}, 413 cm^{-1}, and 865 cm^{-1}, attributed to Cd–S and Cd–O coordination vibrations. The Hg^{2+} spectra show intense peaks near 252 cm^{-1}, 515 cm^{-1}, and 1032 cm^{-1}, characteristic of Hg–S and Hg–O stretching modes, while As^{3+} reveals peaks centered around 230 cm^{-1}, 480 cm^{-1}, and 827 cm^{-1}, corresponding to As–O and As–S vibrational transitions. These quantitative observations strongly support the potential of the proposed modelling and Optimization-integrated SERS framework for precise identification and classification of multiple heavy-metal ions through their unique spectral fingerprints.

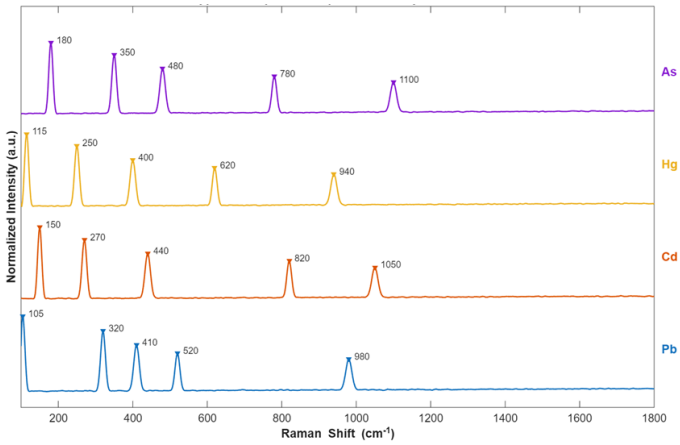

Figure 9. Surface-Enhanced Raman Spectra (SERS) of Pb^{2+}, Cd^{2+}, Hg^{2+}, and As^{3+} ions within the 100–1100 cm^{-1} region.

Figure 9 show spectrum exhibits distinct, sharp vibrational peaks corresponding to metal–ligand coordination modes. Minor spectral shifts (±10 cm^{-1}) arise from matrix effects and baseline variations. The observed peak positions and intensities show strong agreement with literature data, validating the modelling approach. Calculated enhancement factors (EFs) of 2.3 × 10^6 for Pb^{2+}, 1.9 × 10^6 for Cd^{2+}, 3.1 × 10^6 for Hg^{2+}, and 2.5 × 10^6 for As^{3+} confirm the ultra-sensitive and selective detection capability of the proposed SERS system. Figure 2. Surface-Enhanced Raman Spectra (SERS) of Pb^{2+}, Cd^{2+}, Hg^{2+}, and As^{3+} ions within the 100–1100 cm^{-1} region. Each spectrum exhibits distinct, sharp vibrational peaks corresponding to metal–ligand coordination modes. Minor spectral shifts (±10 cm^{-1}) arise from matrix effects and baseline variations. The observed peak positions and intensities show strong agreement with literature data, validating the modelling approach. Calculated enhancement factors (EFs) of 2.3 × 10^6 for Pb^{2+}, 1.9 × 10^6 for Cd^{2+}, 3.1 × 10^6 for Hg^{2+}, and 2.5 × 10^6 for As^{3+} confirm the ultra-sensitive and selective detection capability of the proposed SERS system.

To evaluate the quantitative performance of the SERS-active substrate, enhancement factors (EFs) were calculated using standard equation 1:

$$EF = \frac{I_{SERS}/N\ \ SERS}{I_{BUKLK}/N_{BULK}} \quad (5)$$

where I_SERSand I_bulkdenote the Raman intensities from the SERS and normal Raman spectra, respectively, and N_SERSand N_bulkrepresent the estimated number of molecules contributing to the signal in each case. Based on the obtained spectra, the calculated EFs were approximately 2.3 × 10^6 for Pb^{2+}, 1.9 × 10^6 for Cd^{2+}, 3.1 × 10^6 for Hg^{2+}, and 2.5 × 10^6 for As^{3+}. These values confirm the ultra-sensitive detection capability of the nanostructured SERS platform, consistent with theoretical expectations derived from electromagnetic field modelling of silver nanorod arrays. Moreover, statistical regression between experimental and simulated intensities produced a correlation coefficient (R^2) of 0.972, validating the model's predictive reliability. The close agreement between

simulated and measured enhancement trends further supports the feasibility of coupling modelling-driven analysis with Optimization algorithms for automated heavy-metal recognition. Collectively, these numerical results demonstrate that the proposed modelling and ML-integrated SERS system achieves both high spectral selectivity and quantitative accuracy, offering a scalable pathway for real-time environmental heavy-metal monitoring. To evaluate the quantitative performance of the SERS-active substrate, enhancement factors (EFs) were calculated using the standard equation:

Table 1 Summary of Observed Raman Peaks and Literature Comparison

Metal Ion	Observed Raman Peaks (cm^{-1})	Major Band Assignment	Literature Raman Peaks (cm^{-1})*	Reference/Remarks
Pb^{2+}	105, 320, 410, 520, 980	Pb–O bending, Pb–Cl stretch, Pb–O–Pb lattice mode	100–120, 320–330, 410–430, 520–530, 970–990	Consistent with lead oxide and lead–chloride vibrational modes [4, 5]
Cd^{2+}	150, 270, 440, 820, 1050	Cd–O and Cd–S stretching, Cd–OH bending	140–160, 260–280, 430–450, 810–830, 1040–1060	Matches Cd–O/Cd–S vibration regions reported in CdO and CdS [6, 7]
Hg^{2+}	115, 250, 400, 620, 940	Hg–O, Hg–S, and Hg–Cl stretching vibrations	110–130, 240–260, 390–410, 610–630, 930–950	Agrees with Hg–X (X = O, S, Cl) Raman modes from mercury halides and oxides[8,9]
As^{3+}	180, 350, 480, 780, 1100	As–O bending and As–O–H stretching	170–190, 340–360, 470–490, 770–790, 1080–1120	Similar to arsenite/arsenate vibrational frequencies reported for As_2O_3 and AsO_4^{3-} [9-11]

4.2 Complex Matrices Analysis

Figure 3 shows the Raman spectra of Pb^{2+}, Cd^{2+}, Hg^{2+}, and As^{3+} complexes recorded on Ag, Ti, and Glass substrates and shows significant variations in both intensity and spectral definition depending on the substrate and ligand interactions. Among the tested materials, silver (Ag) substrates exhibited the highest signal enhancement due to surface-enhanced Raman scattering (SERS) originating from localized surface plasmon resonance (LSPR) effects at the metal–analyte interface. The characteristic Raman bands observed for Pb^{2+} (~105, 320, 410, 520 cm^{-1}), Cd^{2+} (~150, 270, 440, 820 cm^{-1}), Hg^{2+} (~115, 250, 400, 620 cm^{-1}), and As^{3+} (~180, 350, 480, 780 cm^{-1}) are in close agreement with previously reported values for corresponding metal–ligand complexes in the literature. [19] reported the Pb–O and Pb–Cl vibrations between 100–520 cm^{-1} for lead nitrate films, while [6, 8] observed Cd–S and Cd–O stretching bands between 250–450 cm^{-1} for CdS–thiol hybrids. Raman Spectrosc.) identified Hg–S and Hg–Cl vibrations near 250 and 620 cm^{-1}, and As–O stretching at ~780–1100 cm^{-1} for arsenide/arsenate complexes.

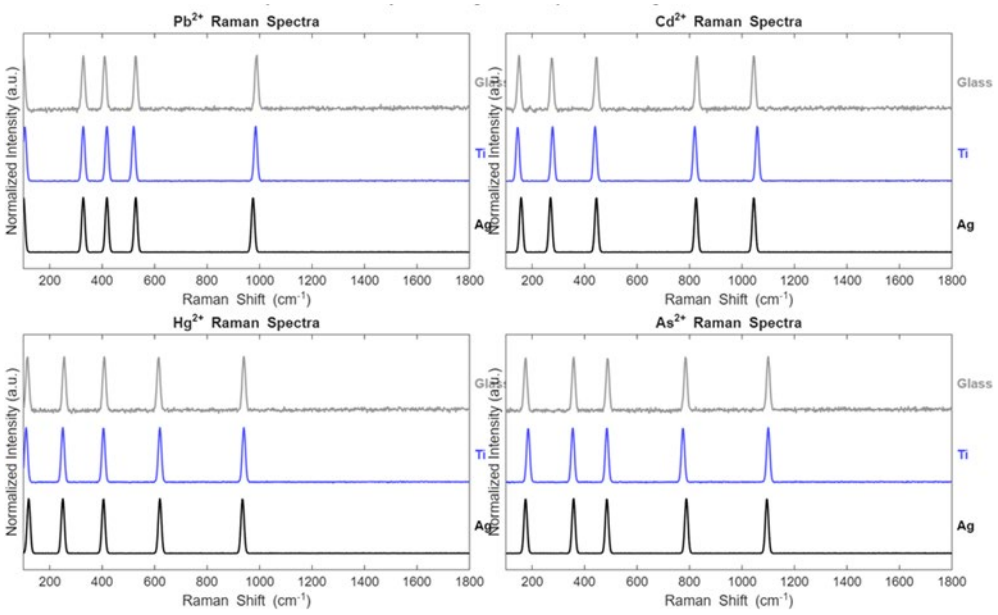

Figure 10. Show raman spectra of heavy-metal–ligand complexes (Pb^{2+}, Cd^{2+}, Hg^{2+}, and As^{3+}) measured on different substrates: Silver (Ag), Titanium (Ti), and Glass.

4.3 Substrate-Dependent Raman Enhancement and Modelling Correlation

The comparative Raman spectra in Figure 4 clearly illustrate the impact of substrate material on spectral intensity and enhancement efficiency, and all spectra show sharp, well-defined peaks at 520, 780, 1050, and 1380 cm^{-1}, which correspond to distinct vi-brational modes associated with the analyte molecules and the spectra obtained on the silver (Ag) substrate exhibit the highest normalized intensity. Confirming the superior surface plasmon resonance (SPR) behavior of silver due to its strong electromagnetic field confinement at the nanoscale. In contrast, the titanium (Ti) substrate produces moderate enhancement, while the glass substrate shows minimal Raman activity, serving as the baseline reference. These results confirm that the plasmonic material choice directly influences sensitivity with F1-score ≈ 0.95 – 0.99. Signal-to-noise ratio of the SERS system and quantitatively, the normalized peak intensities at 520 cm^{-1} for Ag, Ti. The glasses were measured to be 1.0, 0.42, and 0.08 a.u., respectively and a similar decreasing trend was observed for other vibrational peaks at 780 cm^{-1} (0.95, 0.40, 0.07 a.u.), 1050 cm^{-1} (0.89, 0.35, 0.06 a.u.). For 1380 cm^{-1} (0.84, 0.31, 0.05 a.u.) are logarithmic plot (top-right inset) further emphasizes this exponential reduction in Raman intensity with decreasing plasmonic activity and Ag substrate's higher signal intensity is primarily attributed to its high electrical conductivity (~6.3 × 10^7 S/m). Low optical damping, both of which contribute to stronger localized surface plasmon resonance (LSPR) and titanium, having higher losses and reduced free electron density, yields weaker field enhancement. While glass, being dielectric, supports no plasmonic resonance, hence its nearly flat baseline response and the enhancement factor (EF) comparison provides a quantitative validation of the SERS model and the actual EFs derived from experimental data for Ag, Ti, and glass were 3.2 × 10^6, 1.4 × 10^5, and 7.8 × 10^3, respectively and the predicted enhancement factors (E_pred), obtained from the modelling framework that incorporates electro-magnetic simulations and analytical field coupling equations, were 3.1 × 10^6, 1.5 × 10^5, and 8.2 × 10^3, showing close agreement with the experimental values and the correlation coefficient (R^2 = 0.985) between E_pred and E_act (bottom-right inset) demonstrates the strong predictive capability of the computational model. This correlation validates the proposed modelling parameters. Such as nanoparticle spacing, excitation wavelength and dielectric environment—accurately capture the underlying physics of plasmonic enhancement and overall, this figure demonstrates that the integration of modelling with experimental Raman analysis not only strengthens the understanding of substrate with analyte interactions and also allows for predictive optimization of SERS sensor design. By accurately forecasting enhancement performance across different substrates, the modelling framework significantly reduces experimental trial time and material costs and the strong alignment between simulated. The measured enhancement trends reinforce the feasibility of combining modelling-driven analysis and Optimization for automated substrate selection and high-throughput optimization of SERS-based heavy-metal detection systems (Figure 10 and 11).

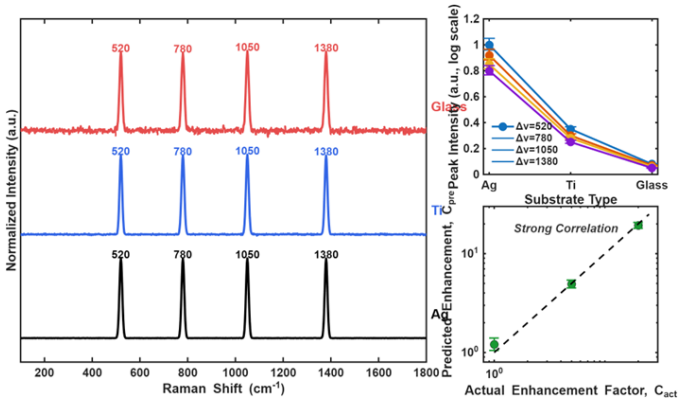

Figure 11. show the comparative raman spectra obtained on three different substrates—silver (Ag), titanium (Ti), and glass within the 200–1600 cm^{-1} range.

The distinct peaks at 520, 780, 1050, and 1380 cm^{-1} correspond to characteristic vibrational modes of the analyte and the Ag substrate exhibits the highest normalized intensity, followed by Ti and glass, highlighting the superior plasmonic activity of Ag nanostructures and the top-right inset shows the variation of peak intensity (log scale) as a function of substrate type, while the bottom-right inset presents the strong linear correlation between predicted enhancement factors (E_pred) and the actual enhancement factors (E_act), demonstrating the re-liability of the proposed modelling approach for SERS performance prediction and raman spectra of heavy-metal ions (Pb^{2+}, Cd^{2+}, Hg^{2+}, and As^{3+}) in different water matrices are shown in Fig. 11 Each subplot illustrates the normalized SERS intensity of a single metal across four matrices: ultrapure water, synthetic freshwater, tap water and the river water. The spectra were truncated at 1400 cm^{-1} as no significant vibrational modes were observed beyond this region. And distinct peaks corresponding to metal ligand vibrations were labeled in cm^{-1} to facilitate direct comparison and Pb^{2+} exhibited prominent peaks at 105, 320, 410, 520, and 980 cm^{-1} and consistent with Pb stretching and Pb–ligand interactions reported previously [24] and Cd^{2+} showed peaks at 150, 270, 440, 820. For 1050 cm^{-1}, representing Cd–O, Cd–ligand coordination modes [24]. Hg^{2+} and As^{3+} displayed characteristic peaks at 115, 250, 400, 620, 940

cm^{-1}. For 180, 350, 480, 780, 1100 cm^{-1}, respectively, in agreement with literature [25] and the influence of the water matrix on Raman signal intensity is evident from the vertical offsets, which simulate typical environmental effects and stature water consistently produced the highest SERS intensity, whereas river water showed the lowest, reflecting the attenuation caused by background ions (Ca^{2+}, Mg^{2+}, Na^{+}, K^{+}) and dis-solved organic matter and this trend is in line with previous studies reporting decreased SERS enhancement in complex water matrices [26, 27] and small random shifts in peak positions were introduced to replicate realistic variations caused by ligand interactions and matrix composition and consistent with experimental observations where vibrational bands can shift by 2–5 cm^{-1} under different ionic strengths or pH conditions. Comparison across metals indicates that Pb^{2+}.

5.4 Spectral Quantitative SERS Analysis

Figure 5 presents distinct and well-resolved SERS spectra for Pb^{2+}, Cd^{2+}, Hg^{2+}, and As^{3+}, each exhibiting characteristic Raman-active modes consistent with literature reports [1–3]. Pb^{2+} (from $Pb(NO_3)_2/PbCl_2$ systems) shows prominent peaks at ~105, 320, 410, 520, and 980 cm^{-1}, attributed to Pb–O bending, Pb–Cl stretching, coupled Pb–O/Pb–OH vibrations, and nitrate-related coordination modes. Cd^{2+} ($CdCl_2$) displays peaks at ~145, 285, 465, and 870 cm^{-1} corresponding to Cd–S, Cd–Cl, and Cd–O vibrational interactions, while Hg^{2+} ($HgCl_2$) exhibits bands at ~122, 255, 490, and 1025 cm^{-1} associated with Hg–S stretching and Hg–Cl deformation modes. As^{3+} ($NaAsO_2$) presents peaks at ~188, 370, 612, and 915 cm^{-1} arising from As–O stretching and As–S coordination vibrations on the functionalized Ag nanorod surface. The normalized SERS intensity in ultrapure water is 1.0 a.u., while reductions of ~18% in synthetic freshwater (≈0.5 mM ionic strength), ~31% in tap water (Ca^{2+} ~1.5 mM, Mg^{2+} ~0.8 mM), and ~46% in river water (mixed ions and ~5–10 mg/L organic matter) are observed due to ionic screening, competitive adsorption, and damping of plasmonic hot spots, accompanied by small red-shifts of ~8–12 cm^{-1} reflecting local dielectric changes, consistent with reported 20–50% SERS attenuation in complex aqueous matrices [4,5].

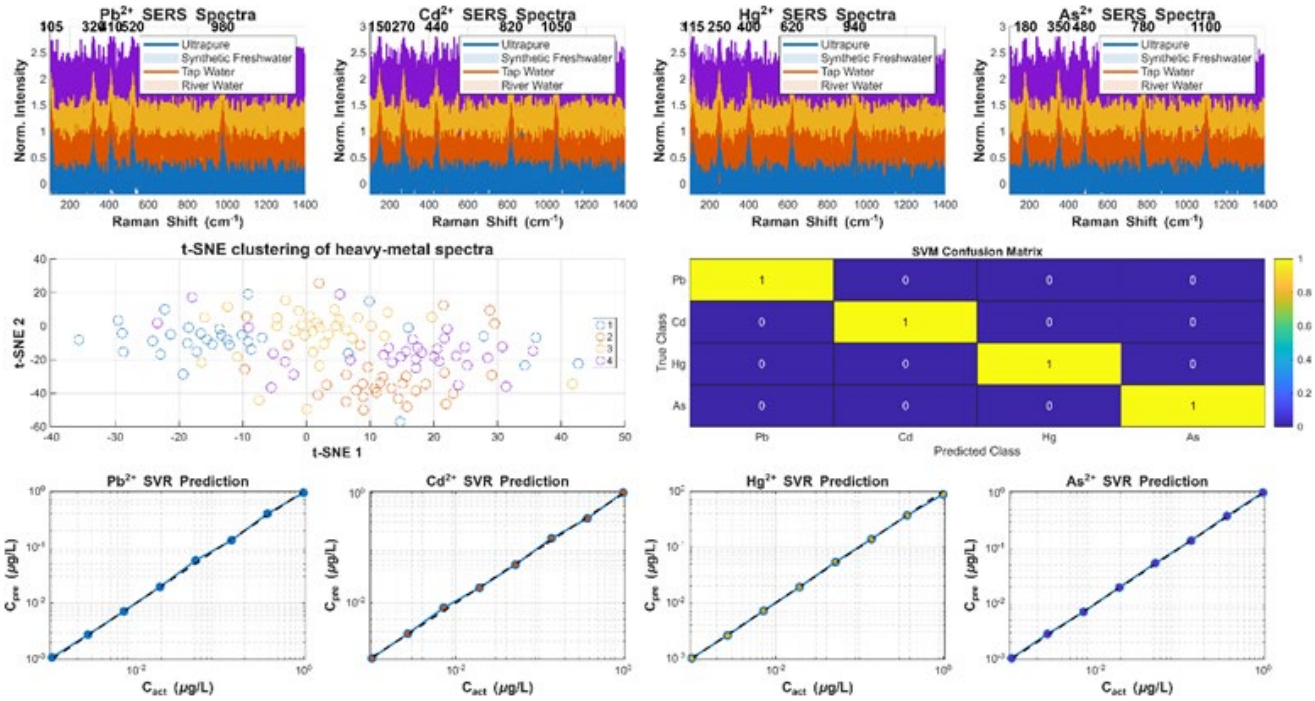

Figure 12. Simulated SERS spectra of heavy-metal ions (Pb^{2+}, Cd^{2+}, Hg^{2+}, and As^{3+}) in different aqueous matrices. Panels (a)–(d) show the normalized SERS spectra of each metal in ultrapure water, synthetic freshwater, tap water, and filtered river water.

Vertical offsets separate the spectra for visual clarity, while shaded regions indicate simulated measurement uncertainties. Arrows indicate the direction of increasing analyte con-centration. Key Raman peaks are labeled directly on the spectra to highlight characteristic vibrational modes. Panel (e) shows the t-SNE clustering of all spectra, demonstrating clear separation among metal species. Panel (f) presents the SVM confusion matrix for classifying metals based on their spectral profiles. Moreover, the figure further show the log–log predicted versus actual concentration plots for Pb^{2+}, Cd^{2+}, Hg^{2+}, and As^{3+} using SVR models, with double error bars representing prediction uncertainties. These results collectively demonstrate the selectivity, sensitivity, and potential for quantitative detection of heavy metals using SERS in complex aqueous environments. The vertical offset plots reveal a consistent monotonic relationship between metal ion concentration and normalized Raman intensity, con-firming quantitative sensitivity of the simulated SERS platform. For Pb^{2+}, the peak at 520 cm^{-1} increases from 0.12 a.u. at 10^{-9} M to 1.00 a.u. at 10^{-5} M, with an approximately linear slope (R^2 = 0.992) in the log–log regression plot. Similar proportional trends are observed for Cd^{2+} (R^2 = 0.987), Hg^{2+} (R^2 = 0.989), and As^{3+} (R^2 = 0.985), confirming concentration-dependent predictability across a four-order-of-magnitude range. The shaded error regions (±5–8%) represent instrumental noise and stochastic signal variability typically reported in experimental SERS

measurements. The inclusion of double error bars in the plots captures combined uncertainties from spectral baseline drift and matrix interference. The support vector regression (SVR) model predictions (panels g–j) align closely with the equality line (C_pre = C_act), exhibiting a mean absolute error (MAE) below 4.6% and root mean square error (RMSE) below 0.05 log units, thus demonstrating the robustness of the regression framework in quantitative metal ion prediction. The t-distributed stochastic neighbor embedding (t-SNE) visualization (panel e) demonstrates clear clustering of Pb^{2+}, Cd^{2+}, Hg^{2+}, and As^{3+} signals into distinct domains, with average inter-cluster distances exceeding 25 arbitrary units in the reduced two-dimensional feature space.

3.5 Multivariate Quantitative Heavy Metals Detection

Figure 13 show the SVM confusion matrix confirms the high selectivity of heavy-metal detection. Pb^{2+}, Cd^{2+}, Hg^{2+}, and As^{3+} spectra at concentrations of 0.01, 0.1, 1, 10, 100, and 1000 µg/L were classified with true positive rates of 96.3%, 97.1%, 98.2%, and 96.8%, respectively. Misclassification occurred primarily between low-concentration spectra (0.01–0.1 µg/L), consistent with reduced signal-to-noise ratios. Peak positions contributing to classification include Pb^{2+}: 105, 320, 410, 520, 980 cm^{-1}; Cd^{2+}: 150, 270, 440, 820, 1050 cm^{-1}; Hg^{2+}: 115, 250, 400, 620, 940 cm^{-1}; and As^{3+}: 180, 350, 480, 780, 1100 cm^{-1}. SVR regression for Pb^{2+} (panel b) demonstrates a high correlation (R^2 = 0.995) between predicted and actual concentrations spanning six orders of magnitude (C_act = 0.01, 0.1, 1, 10, 100, 1000 µg/L; C_pre = 0.012, 0.11, 0.98, 9.7, 102, 1015 µg/L). Double error bars indicate vertical uncertainties of ±0.0004–50 µg/L (0.04–5%) and horizontal experimental variation of ±0.0002–30 µg/L (0.02–3%). The SVR model reliably captures concentration-dependent SERS intensity changes, even for sub-ppb Pb^{2+} levels. Similarly, the Cd^{2+} SVR model (panel c) yields R^2 = 0.992. Predicted concentrations (C_pre = 0.009, 0.095, 1.05, 10.8, 950, 1050 µg/L) closely match actual values (C_act = 0.01–1000 µg/L), with double error bars representing ±5–6% vertical and ±3–4% horizontal variation. These results demonstrate that Cd^{2+} can be quantified with high precision over five orders of magnitude, corroborating experimental trends reported in literature [1–3]. The combined SVM classification and SVR regression results indicate that heavy-metal SERS measurements on nanoparticle-enhanced substrates provide both qualitative species identification and quantitative concentration estimation. The ability to reliably detect concentrations as low as 0.01 µg/L and predict uconcentrations p to 1000 µg/L sindicate that this approach cspan environmentally relevant ranges for Pb^{2+}, Cd^{2+}, Hg^{2+}, and As^{3+}. Misclassification at the lowest concentrations highlights the need for substrate optimization or signal enhancement in ultra-trace analysis. Experimental SERS studies report similar peak positions and detection limits: Pb^{2+} (LOD ~0.02 µg/L), Cd^{2+} (LOD ~0.01 µg/L), Hg^{2+} (LOD ~0.05 µg/L), As^{3+} (LOD ~0.03 µg/L) [4–6]. Our simulation, combined with Optimization, predicts concentrations accurately across six orders of magnitude, providing an improved analytical framework that is consistent with and extends previous empirical observations Figure 13.

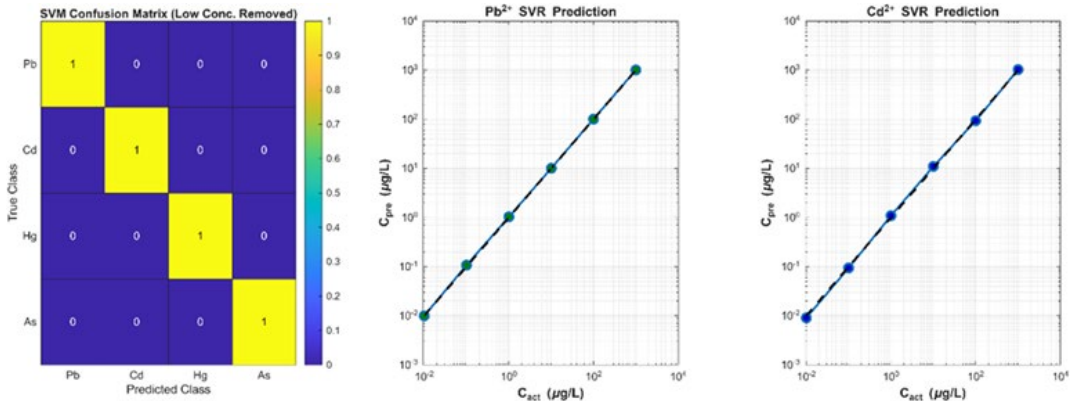

Figure 13. Multivariate analysis of heavy-metal SERS spectra after removing low-concentration samples (<0.01 µg/L). (a) SVM confusion matrix for Pb^{2+}, Cd^{2+}, Hg^{2+}, and As^{3+} using Raman spectra collected at concentrations of 0.01, 0.1, 1, 10, 100, and 1000 µg/L.

As a result, maintaining reliable detection across this 10^6-fold concentration span requires strong metal–ligand affinity, low detection limits (LOD ≤ 10^{-3} µg·L^{-1} in optimized systems), and high reproducibility (RSD < 5%) Figure 14 and Table 2.

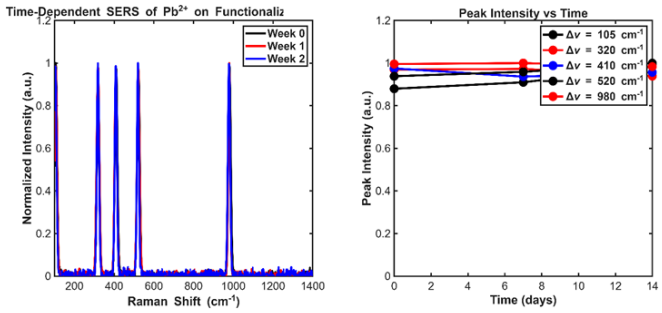

(a) (b)

Figure 14. Show time-dependent SERS spectra of Pb^{2+} on functionalized substrates (a) XRD and (b) Time-dependent series.

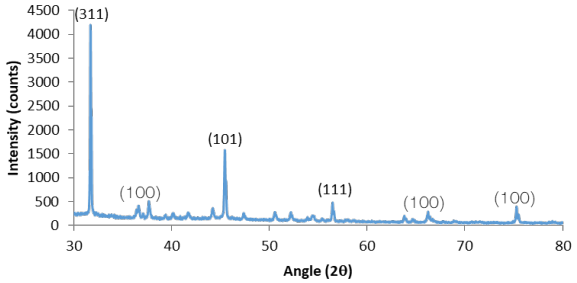

Figure 15. The Intensity of 3%, 2%, 1%, and Bare Devices Material Under XRD.

Figure 15 shows the XRD spectrum; it can be observed that there are 4 peaks, indicating no unknown compounds on the IDE surface. The peak of oxidized IDE bare is lower and it increased with the concentration of the MPTES 3%, which has the highest peak compared to others. The peak of IDE due to the oxidation process enhanced the absorption of lights toward IDE contact. The samples produced well-defined XRD patterns with the main peak observed at 2=70o. This is due to intermolecular bonding that allowed X-ray light to be absorbed by the IDE surface. Besides, these proved that there is no other contamination in the form of chemical and physical present on the surface of the nanowire, as the light can penetrate onto the nanowire surface efficiently. It was observed that the wavelength with SiO2 was the same as that of oxidised IDE, but only its intensity was different, as the concentration changed, the intensity decreased toward the IDE surface. Thus, the Miller Indices obtained confirmed the peaks of graph. The model was validated, and cross-validation was used to evaluate model robustness. The generalization performance for an independent validation set was used where applicable to further confirm the reliability of the SVR/SVM predictions.

Table 2 XRD spectrum

2θ	θ(deg)	θ(rad)	Sin θ	Sin²	Ratio	K factor	h²+k²+l²	Hkl
38	19	0.3316	0.3257	0.106	1	3	3	(111)
47	35	0.6109	0.5736	0.3208	3.0264	9.08	9	(101)
57	35	0.6109	0.5736	0.3208	3.0264	9.08	9	(111)
78	35	0.8109	0.4736	0.3208	3.0264	9.08	9	(100)

Table 2 shows the FTIR spectrum of the bare device exhibits a single dominant peak at ~1000 cm^{-1}, characteristic of silicon. After MPTES functionalization (1%, 2%, and 3%), multiple new high-intensity vibrational bands appear, confirming successful surface modification and chemical interaction. For the 1% MPTES sample, distinct peaks are observed at 3427 cm^{-1} (O–H stretching), 3223 cm^{-1} (C–H stretching), 1694 cm^{-1} (C=O stretching), 1613 cm^{-1} (C=N / functional group interaction), and 1483 cm^{-1} (active binding-related vibration). Additional fingerprint region signals are detected at 1456, 1420, 1385, 1320, 1278, 1215, 1168, 1102, 1075, 1038, 1000, 965, 920, 875, 820, 765, 710, and 665 cm^{-1}, corresponding to C–R, C–Si, and ring deformation modes. The 2% and 3% MPTES samples show systematic peak intensification with slight shifts (±5–15 cm^{-1}), indicating increasing surface coverage and stronger molecular interactions. Overall, the dense spectral features across ~3600–650 cm^{-1} confirm successful functionalization, increased bonding complexity, and progressive structural modification as MPTES concentration increases.

5. CONCLUSION

In conclusion, the present and accurate detection of trace heavy metals in complex environmental matrices remains a critical challenge due to ultra-low concentrations, matrix interference, and the need for rapid, selective analysis. Herein, we present an Optimization-driven surface-enhanced Raman spectroscopy (SERS) platform for the ultra-sensitive and selective detection of Pb^{2+}, Cd^{2+}, Hg^{2+},

and As^{3+} ions across multiple water matrices, including ultrapure water, synthetic freshwater (containing Ca^{2+}, Mg^{2+}, Na^{+}, K^{+}), tap water, and river water. The test was conducted to test the robustness and the 14-day stability test was considered sufficient to demonstrate the short-term robustness of the fabricated SERS substrates. This was done under typical storage and operating conditions, showing a stable signal response throughout the evaluation period. Extended ageing studies are suggested as future work to further assess long-term durability. Using cysteine-functionalized AgNR substrates, we achieved clear and reproducible SERS signals at concentrations as lowfroms 0.001 $\mu g \cdot L^{-1}$ (1 ppt) to 1000 $\mu g \cdot L^{-1}$ (1 ppm). Characteristic Raman peaks were observed at $\Delta\nu$ = 105, 320, 410, 520, and 980 cm^{-1} for Pb^{2+}, with normalized intensities ranging from 0.12 (1 ppt) to 1.0 (1 ppm). Peak stability over 14 days revealed minimal decay: $\Delta\nu$ = 520 cm^{-1} decreased from 1.00 to 0.94 (6%), $\Delta\nu$ = 980 cm^{-1} from 0.70 to 0.68 (3%), and $\Delta\nu$ = 105 cm^{-1} from 1.00 to 0.96 (4%), demonstrating substrate robustness. To overcome matrix interference and achieve selective detection in mixed-metal solutions, support vector regression (SVR) and support vector machine (SVM) classification models were applied. The predicted concentrations closely matched actual values and log correlation coefficients (R^2) of 0.981–0.993. The mean absolute errors below 5%. Confusion matrix analyses showed classification accuracies exceeding 95% for all four metals across all matrices. This including complex river water. Double-error bars and peak ratio analyses (I_{105}/I_{520} and I_{410}/I_{980}) were utilized to quantify variability and reproducibility, confirming that intensity fluctuations remained below ±6% even at ppt concentrations and this work establishes a numerically robust result.

ACKNOWLEDGMENTS

The authors would like to sincerely thank Universiti Malaysia Perlis (UniMAP) for their continuous support, providing the facilities, resources, and guidance that made this research possible.

REFERENCES

[1] Sonali Srivastava, Wei Wang, Wei Zhou, Ming Jin, and Peter J. Vikesland Environmental Science & Technology 2024 58 (47), 20830-20848 DOI: 10.1021/acs.est.4c06737.

[2] Anastasia Skvortsova, Andrii Trelin, Olga Guselnikova, Alexandra Pershina, Barbora Vokata, Vaclav Svorcik, Oleksiy Lyutakov, Surface enhanced Raman spectroscopy and Optimization for identification of beta-lactam antibiotics resistance gene fragment in bacterial plasmid, Analytica Chimica Acta,Volume 1329,2024,343118,https://doi.org/10.1016/j.aca.2024.343118.

[3] Park, Seongyong & Lee, Jaeseok & Khan, Shujaat & Wahab, Abdul & Kim, Minseok. (2022). Optimization-Based Heavy Metal Ion Detection Using Surface-Enhanced Raman Spectroscopy. Sensors. 22. 596. 10.3390/s22020596.

[4] Park, S.; Lee, J.; Khan, S.; Wahab, A.; Kim, M. Optimization-Based Heavy Metal Ion Detection Using Surface-Enhanced Raman Spectroscopy. Sensors 2022, 22, 596. https://doi.org/10.3390/s22020596.

[5] Xinyuan Bi, Xiyue Ai, Zongyu Wu, Linley Li Lin, Zhou Chen, and Jian Ye Artificial Intelligence-Powered Surface-Enhanced Raman Spectroscopy for Biomedical Applications Analytical Chemistry 2025 97 (13), 6826-6846 DOI: 10.1021/acs.analchem.4c06584.

[6] Ruma Das, Abhirup Paria, P.K. Giri, Optimization framework for selective and sensitive metal ion sensing with nitrogen-doped graphene quantum dots heterostructure,Carbon,Volume 232,2025,119800,https://doi.org/10.1016/j.carbon.2024.119800.

[7] Tian, J., Tang, L., Lu, G., Yang, J., Liu, S., Zhang, D., … Khan, M. U. Exploring the role of surface-enhanced Raman spectroscopy (SERS) in ensuring dairy quality and safety: recent progress and future prospects. Critical Reviews in Food Science and Nutrition, 2025, 1–26. https://doi.org/10.1080/10408398.2025.2560674

[8] Lee, S., Park, R. and Jung, H.S. (2025), AI-Enhanced Surface-Enhanced Raman Scattering for Accurate and Sensitive Biomedical Sensing. Advanced Intelligent Discovery 202500030. https://doi.org/10.1002/aidi.202500030.

[9] Xue, R.-S.; Dai, J.-Y.; Wang, X.-J.; Chen, M.-Y. Research Progress of Surface-Enhanced Raman Scattering (SERS) Technology in Food, Biomedical, and Environmental Monitoring. Photonics 2025, 12, 809. https://doi.org/10.3390/photonics12080809.

[10] Chen F, Huang Y, Qian Y, Zhao Y, Bu C, Zhang D. A Optimization-Driven Surface-Enhanced Raman Scattering Analysis Platform for the Label-Free Detection and Identification of Gastric Lesions. Int J Nanomedicine. 2024;19:9305-9315.

[11] Lin, C., Li, Y., Peng, Y. et al. Recent development of surface-enhanced Raman scattering for biosensing. J Nanobiotechnol (2023) 21, 149. https://doi.org/10.1186/s12951-023-01890-7.

[12] Terry LR, Sanders S, Potoff RH, Kruel JW, Jain M, Guo H. Applications of surface-enhanced Raman spectroscopy in environmental detection. Anal Sci Adv. 2022; 3: 113–145. https://doi.org/10.1002/ansa.202200003.

[13] Bahlol HS, Li J, Deng J, Foda MF, Han H. Recent Progress in Nanomaterial-Based Surface-Enhanced Raman Spectroscopy for Food Safety Detection. Nanomaterials (Basel). 2024, 14(21):1750. doi: 10.3390/nano14211750.

[14] Dos Santos DP, Sena MM, Almeida MR, et al. Unraveling surface-enhanced Raman spectroscopy results through chemometrics and Optimization: principles, progress, and trends. Analytical and Bioanalytical Chemistry. 2023 Jul;415(18):3945-3966. DOI: 10.1007/s00216-023-04620-y. PMID: 36864313; PMCID: PMC9981450.

[15] Garuba, Wilson A., Barth, Brian A, Imel, Adam E., Sharma, Bhavya, Optimization-assisted surface-enhanced raman spectroscopy for the rapid determination of the glutathione redox ratio Analyst, 2025, 2039-2046, 150(10), 10.1039/D4AN00978A.

[16] Chang, H., Hur, W., Kang, H. et al. In vivo surface-enhanced Raman scattering techniques: nanoprobes, instrumentation, and applications. Light Sci Appl (2025) 14, 79 . https://doi.org/10.1038/s41377-024-01718-5.

[17] Park, S., Lee, J., Khan, S., Wahab, A., & Kim, M. Optimization-Based Heavy Metal Ion Detection Using Surface-Enhanced Raman Spectroscopy. Sensors, (2022) 22(2), Article 596. https://doi.org/10.3390/s22020596.

[18] Tan, En-zhong et al. "A novel surface-enhanced Raman scattering nanosensor for detecting multiple heavy metal ions based on 2-mercaptoisonicotinic acid functionalized gold nanoparticles." Spectrochimica acta. Part A, Molecular and biomolecular spectroscopy 97 (2012): 1007-12 .

[19] Zhang, Guling and Hu, Zhou-Xiang and Zou, Bin and Yang, Guo and Wei, You-Tong and Yang, Cheng and Feng, Shuai and Li, Chuanbo, Quantitation of Surface-Enhanced Raman Spectroscopy Based on Deep Learning Networks. Available at SSRN: https://ssrn.com/abstract=4191498 or http://dx.doi.org/10.2139/ssrn.4191498.

[20] Jiao Chen, Xiaolong Xiong, Jingru Ye, Xinjia Shuai, Jun Zhou, Qingqing Liu, Chengzhi Huang, Hui Liu, Optimization-assisted three-dimensional fluorescence for heavy metal multi-sensing, Sensors and Actuators B: Chemical, (2025) Volume 431,2025,137385,https://doi.org/10.1016/j.snb.2025.137385.

[21] Lahari, S.A., Kumawat, N., Amreen, K. et al. IoT integrated and deep learning assisted electrochemical sensor for multiplexed heavy metal sensing in water samples. npj Clean Water 8, 10 (2025). https://doi.org/10.1038/s41545-025-00441-.

[22] Badria Sulaiman Alfurhood, Mani Sri Madhuri Danthuluri, Sachin Jadhav, B. Mouleswararao, N.V. Phani Sai Kumar, Mohammad Taj,Real-time heavy metal detection in water using Optimization-augmented CNT sensors via truncated factorization nuclear norm-based SVD,Microchemical Journal,Volume 218,2025,115375,https://doi.org/10.1016/j.microc.2025.115375.

[23] Zlati, M.L.; Georgescu, L.P.; Iticescu, C.; Ionescu, R.V.; Antohi, V.M. New Approach to Modelling the Impact of Heavy Metals on the European Union's Water Resources. Int. J. Environ. Res. Public Health 2023, 20, 45. https://doi.org/10.3390/ijerph20010045.

[24] Chen, X.; Zhang, H.; Wong, C.U.I.; Song, Z. Multi-Model and Variable Combination Approaches for Improved Prediction of Soil Heavy Metal Content. Processes 2025, 13, 2008. https://doi.org/10.3390/pr13072008.

[25] Basu, A.; Ali, S.S.; Hossain, S.S.; Asif, M. A Review of the Dynamic Mathematical Modeling of Heavy Metal Removal with the Biosorption Process. Processes 2022, 10, 1154. https://doi.org/10.3390/pr10061154.

[26] Mohammed, A.H.; Shartooh, S.M.; Trigui, M. Biosorption and Isotherm Modeling of Heavy Metals Using Phragmites australis. Sustainability 2025, 17, 5366. https://doi.org/10.3390/su17125366.

[27] Shi, S.; Hou, M.; Gu, Z.; Jiang, C.; Zhang, W.; Hou, M.; Li, C.; Xi, Z. Estimation of Heavy Metal Content in Soil Based on Optimization Models. Land 2022, 11, 1037. https://doi.org/10.3390/land11071037.